

MORPHING COMPLIANT TRAILINGEDGE SKIN CONCEPT

J. Tikalsky,

Institute of Lightweight Systems, German Aerospace Center (DLR), 38108 Braunschweig,
Germany

Abstract

Many different concepts for morphing trailing edges (TE) have been investigated during the last decades. Within the internal project morphAIR (Morphing Technologies & Artificial Intelligence Research Group) the German Aerospace Center (DLR) is planning further steps by investigating morphing technologies in scaled flight tests. In these flight tests, major effects of morphing technology are going to be shown. Due to having a small-scale demonstrator, former TE concepts need to be evaluated according to applicability, positive lift to drag (L/D) effects and associated weight penalties.

Since large deformations are to be achieved typically in a hingeless-elastic system, high actuation forces are required in order to enable morphing. These internal structural loads are crucial for actuator and kinematic design, thus they are directly related to actuator and kinematic weight. Therefore, it is essential to have a measure of required size and weight during preliminary design processes. Within this work, four different methods are presented to derive the strain energy of a new compliant morphing TE system. Beginning with a geometrical linear analytical approach considering small deformations (Model I), over a nonlinear analytical approach incorporating large deformations (Model II), to geometric nonlinear Finite Element Method (FEM) calculations without (Model III) as well as including Fluid Structure Interaction (FSI) (Modell IV).

Results of Modell I to IV are compared according to strain energy and virtual Forces. It has been shown that even Model I shows good correlation of deformations and strain energy.

1. KEYWORDS

Morphing, Wing, Trailing edge, Strain energy

2. ABBREVIATIONS

AoA	Angle of Attack
Cd	profile Drag coefficient
CD	3D Drag coefficient
Cl	Profile Lift coefficient
CL	Aircraft Lift coefficient
CFRP	Carbon fiber reinforced Plastics
DOF	Degree of Freedom
E	averaged Youngs Modulus
FEM	Finite Element Method
FE	Finite Element
FSI	Fluid Structure Interaction
FRP	Fiber reinforced Plastics
GFRP	Glas fiber reinforced Plastics
HyTEM	Hyperelastic Trailing Edge Morphing
L/D	Lift to drag ratio
TE	Trailing Edge

3. INTRODUCTION AND MOTIVATION

A number of chamber morphing concepts has been developed in the last decades. Most of them have been widely investigated in low- as well as high-fidelity analysis. Some have been investigated in demonstrators and wind tunnels, but only a minority have been tested in flight tests. An Overview of concepts and their level of testing are presented in [1]

As stated only a minority of these concepts have been tested in Flight tests.

Until today, none of that morphing concept is used in the commercial aircrafts even when potentials are widely admitted by experts. The lowering of drag (CD) on wing is predicted to be significant [2]. By increasing Lift at same amount of Drag or by optimizing spanwise Lift distribution.

The gap between Predictions which need to make simplifications and real Flight performance remains open. The Project "MorphAIR" make a first step to close this gap by measure the influence of morphing technology in flight on the top-level aircraft specifications. Using the benefits of a scaled flight test platform, "Proteus" will fly in speed range

of Mach 0.02 – 0.3. This provides a wide flight envelope for performance measurements like flight efficiency and maneuverability.

This paper presents a new compliant trailing edge concept in order to obtain a good compromise between structural stiffness to withstand aerodynamic loads and minimizing actuator loads, which are required to deform the trailing edge. Overcoming different Circumferential (Belt) lengths at every deflection of the system. Is a major challenge if the Profile skins should remain without Gaps. The Provided concept will reduce these internal loads dramatically.

First the Demonstrator will be presented and its Operational Boundaries will be discussed. Then the Hyper elastic trailing edge concept will be presented before a set of 4 different Structural models will be developed. After that Results of all models are compared and discussed.

4. DEMONSTRATOR

The choice of Proteus for as scaled Flight test Platform Provides the Project with a wide range of Speed and CL requirements. Which the wing has to full fill. It can be expected to be impossible to compromise aerodynamic performance in all flight condition with one fixed wing and Profile shape.



Figure 1: DLR unmanned aerial system "Proteus" on run way at National Experimental Test Center of Unmanned Aircraft Systems in Cochstedt

Wing span	2,5	m
Stall speed	75	km/h
Never exceed speed	300	km/h
Maximum take-off weight	30	kg

Maximum speed of 300 km/h will inhibit waves and thus it is impossible to show positive effects to wave drag reduction with this platform. Thus pressure- and induced drag reduction will be focused. Relevant morphing systems are placed on leading – and Trailing Edge to allow chamber modification. To reduce drag at off design flight conditions.

Due to an Average Aspect ratio Lift distribution optimization offers additional Potential for Spanwise differential Morphing systems.

5. DESIGN CONCEPT

As discussed above a number of morphing trailing edge design concepts have been developed and investigated at different technology levels. Common to all concepts are that the skin is discontinuous by elastic means or a sliding mechanism to compensate skin belt changes due to large TE deformation. This leads to potential disturbances, where the transition of laminar into a turbulent flow occurs and therefore the drag increases. Sliding mechanisms are additionally subject to wear. elastic material deviates from target shape in compressed or Elongated situations due to transverse deformation.

In contrast, the Hyperelaststic Trailing Edge Morphing system (HyTEM) combines high deformation with continuous skin on the aerodynamic surfaces. This concept is designated to make use of state-of-the-art and well-known skin materials like fiber reinforced plastics (FRP/GFRP/CFRP) by combining them with a flexural adhesive at the end of the Trailing edge. Which connects suction- and pressure side of the Profile.

This flexural adhesive carry the internal forces and allows large deformations by enabling the TE to change belt length without establishing a sliding mechanism.

Additionally, profile contours can hold gapless and might be a good enabler for laminar flow profiles. Additionally the Flexural behavior of the Adhesive enables Spannwise nonuniform deflections of the TE without increasing Actuator requirements significantly if the Distances of load introduction points is chosen properly.

Every reduction of internal loads and thus potential energy of the deformed mechanism leads to both potentially smaller and lighter actuators as well as to lighter structure due to reduced buckling requirements. So, strain energy is found to be a reliable quantity evaluating this morphing concept without designing actuators and kinematics itself. Concept models of different complexities have been established and compared to evaluate the potentials. The first model is a very simple model and has a high abstraction level. Therefore, it is a low fidelity method. Model I assumes a chain of 3 entities with different stiffnesses and stiffness formulations. Model 2 assumes a geometrical deformation of skins and HyTEM with geometrical linear behavior, but allowing large deformations.

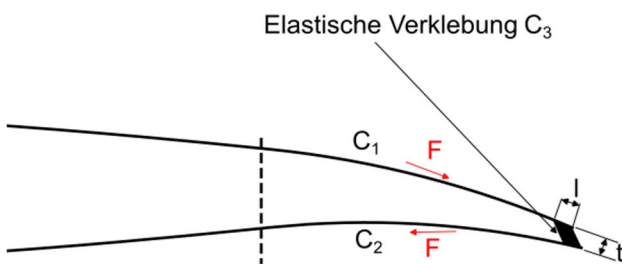
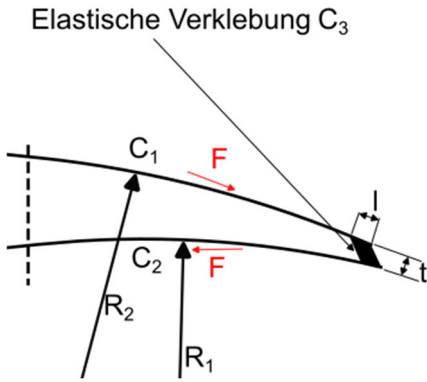
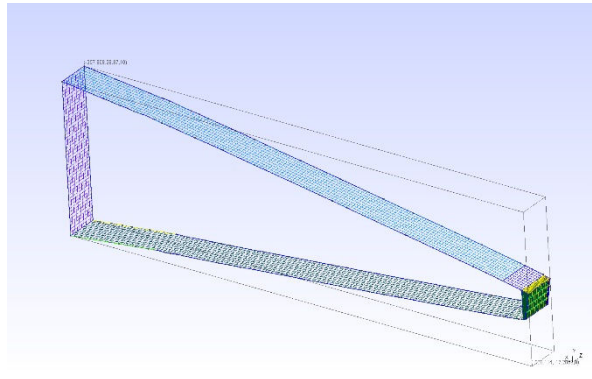
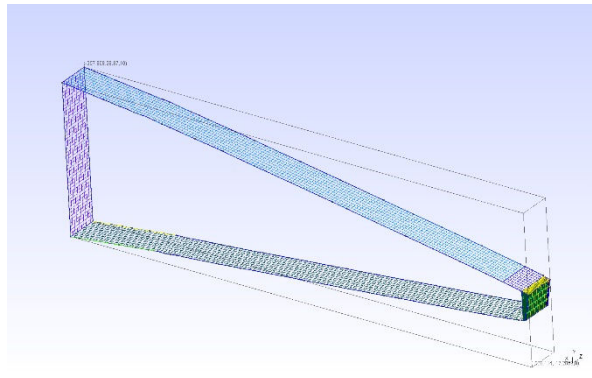


Figure 2: Concept of a Hyperelaststic Trailing Edge Morphing system (HyTEM)

The next one includes a finite element models with geometric non linearities (Model III). This model contains linear elastic behavior of the flexural adhesive. All previous models are considering only internal structural loads induced by a given deformation. So, Model IV is complemented by aerodynamical loads to the skin surfaces. TAB. 1: Trailing Edge Model shows all four models with a sketch for better understanding.

TAB. 1: Trailing Edge Model

	Method	Sketch
Not simplified		
Model I	Geometric linear, small deformations Analytical	

<p>Model II</p>	<p>Geometric linear, small deformations</p> <p>Analytical</p>	
<p>Model III</p>	<p>Geometric nonlinear, large deformations</p> <p>FEM</p>	
<p>Model IV</p>	<p>Geometric nonlinear, large deformations, aerodynamic loads applied</p> <p>FEM</p>	

5.1. Model I

Model I is a top level estimation for the potentials of this Morphing concept considering the internal load relief and there strain energy.

The system is simplified to a linear chain of 3 stiffnesses. Stiffness 1 and 3 are linear elastic spring elements, which represents the skin stiffness. Stiffness 2 represents the trailing edge flexural adhesive as a shear element. Using Δl as known or preset deformation it is possible to determine F as internal force depending to stiffness parameters by the simplified model in Figure 3

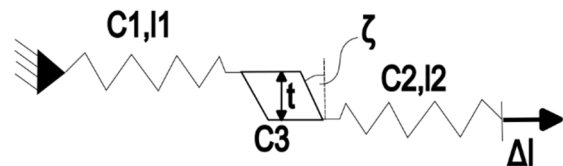


Figure 3: Model I containing springs as skin simplifications and shear element as adhesive

It is necessary to cut the system at the connections of the elements as Figure 4 shows in order to define the static forces at each element.

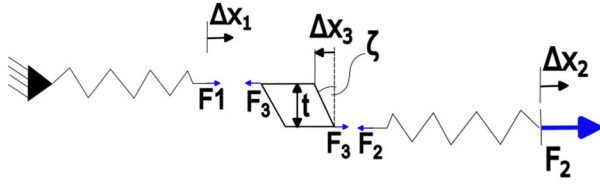


Figure 4: Model I with static forces at each element interface

The linear elastic equations to derive the forces in dependency of deformation can be found in following equations. The sum of deflections has to be the total deformation, which needs to be investigated (1) to (3).

$$(1) F1 = C1 \cdot \Delta x_1$$

$$(2) F2 = C2 \cdot \Delta x_2$$

$$(3) F3 = C3 \cdot \tan(\zeta) \text{ with } \zeta = \arctan\left(\frac{\Delta x_3}{t}\right)$$

$$(4) \Delta l = \Delta x_1 + \Delta x_2 + \Delta x_3$$

By equate formulas (1) and (3) the deflection of each part can be written to be dependent to ζ as:

$$(5) \Delta x_1 = \frac{C3}{C1} \cdot \tan(\zeta)$$

If those values are replaced in equation (1) the total deformation for small values of ζ can be described as in equation (6). By extracting ζ to equation (7) and inserting the result into equation (1) and assuming $C1$ and $C2$ to be equal the force of the system can be derived by equation(8).

$$(6) \Delta l = \tan(\zeta) \left(C3 \left(\frac{1}{C1} + \frac{1}{C2} \right) + t \right)$$

$$(7) \zeta = \arctan\left(\frac{\Delta l}{C3 \left(\frac{1}{C1} + \frac{1}{C2} \right) + t}\right)$$

$$(8) F = C3 \cdot \tan\left(\arctan\left(\frac{\Delta l}{2 \cdot \chi + t}\right)\right) = C3 \frac{\Delta l}{2 \cdot \chi + t} \text{ with } \chi = \frac{C3}{C1}$$

Whereas prescribed before $C1$, $C2$ represent the skin stiffnesses. This is a very low level model approach where no bending and buckling effects as well as stiffness changes due to curvature changes of the skins are considered. The stiffness can be described as following.

$$(9) C1, C2 = \frac{E \cdot t_{laminat}}{l_{skin}}$$

As the shear element stiffness can be prescribed by assuming small deformations as

$$(10) C3 = G \cdot l_{klebung} \quad C1, C2 = \frac{E \cdot t_{laminat}}{l_{skin}}$$

the strain energy is evaluable with a known deformation Δl . This can be geometrically determined as it is shown in Figure 5. The equation can be written as:

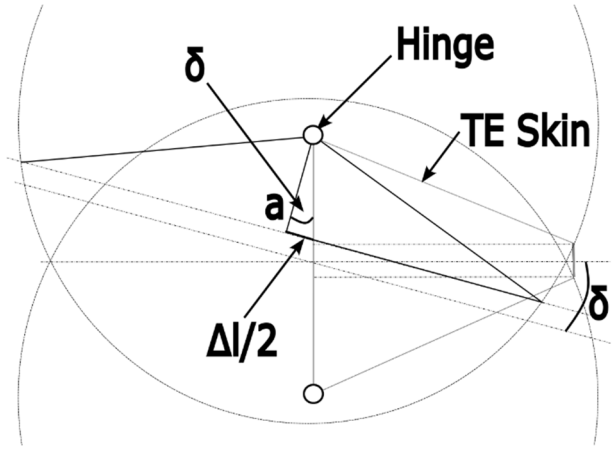


Figure 5: Model I geometrical Trailing edge shear displacement

Strain energy is calculated by

$$(11) L(\delta) = C3 \frac{2 \cdot a \cdot \sin(\delta)}{2 \cdot \chi + t} \text{ with } \chi = \frac{C3}{C1}$$

This leads to a conclusion where the strain energy and thus actuator sizes are geometrically dependent to δ , a , $l_{klebung}$ and t of the of the flexural adhesive. Equation (11) shows that Δl depends of δ and half of the profile thickness, but it is independent to flap length.

5.2. Model II

As Model I have been derived for small deformations and a strong simplification neglecting deformations of the skin. Modell II additionally considers skin deformations and large deformation of the trailing edge Bonding

5.2.1. Deformation determination procedure

As in preliminary design the stiffness and internal loads and their distribution are unknow. It is assumed to deform the upper and lower skin according to sectors of circles with constant arclength. Thus, it is assumed that the bending stiffness is lower than the membrane stiffness of the skins. Furthermore, the circle segments are tangential to upper and lower profile connection point. Furthermore, a constant bonding thickness is assumed. This assumption decouples the internal loads from deformed geometry so the deformed geometry is a direct function of the deflection angle δ .

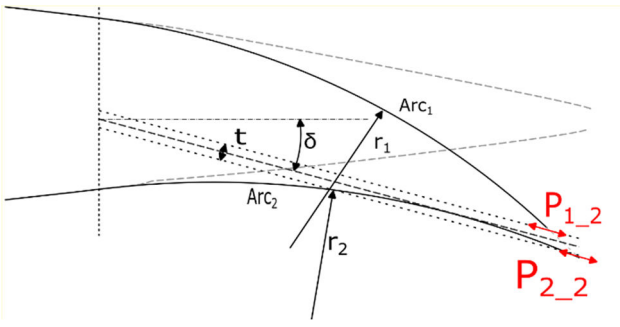


Figure 6: Geometrical properties of model II with solid lines as deformed trailing edge skin and grey dashed line as initial position of the skin

For a given deflection δ and a bonding thickness t the Points P_{1_2} and P_{2_2} can be identified by the intersection of an arc segment with radius r and a given arc length.

Figure 7 shows the solution of deformed (solid blue) and undeformed (dashed blue) trailing edge and their tip trajectories (grey and green). In This example the virtual hinge line is located at 0,75 of chord length. The flexural adhesive thickness is marked by red and purple dotted lines.

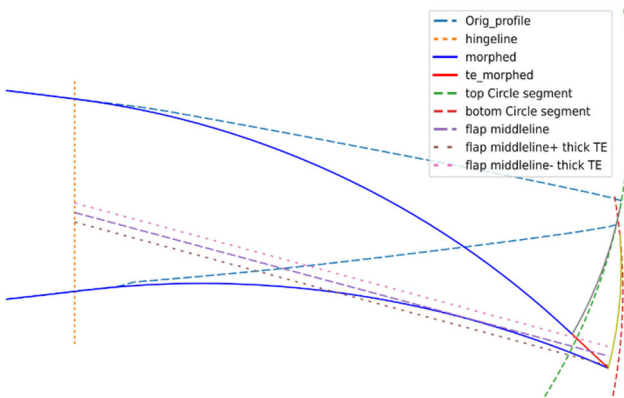


Figure 7: Trajectories model I vs. Model II

It is conspicuous that the form of trajectories in Figure 7 and Figure 5 are in both cases a circle segment. It can be recognized that both trajectories show the same characteristic. The trajectories differ from each other with increasing deflection of the flap. In model II the arc length of skins is constant assuming a much higher membrane stiffness compared to bending stiffness of the skins. As the radius of the Arcs are decreasing the length in Flow direction is shortened compared to model I.

But it can be also recognized that the total difference (Δl) are very close to each other. To make both models comparable the strain energies need to be calculated.

5.2.2. Strain energy of Profile skins

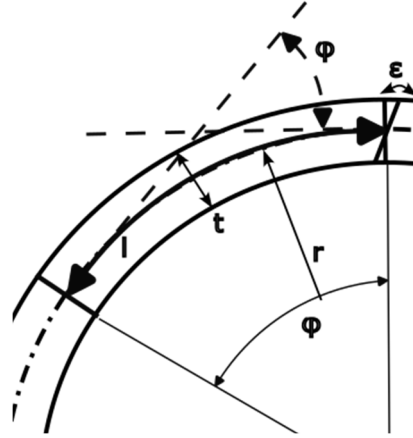


Figure 8: Model II Geometrical skin deformation

As l is hold constant the bending angle ϕ be determent with radius r .

$$(12) \phi = \frac{l}{\pi r}$$

Figure 8shows the geometrical assumption to determine strain ϵ with r and material thickness $t_{laminare}$. The tension of the material can be derived by equation (15).

$$(13) \epsilon = \frac{\pi(r + \frac{t_{laminare}}{2})}{\pi r}$$

$$(14) \sigma = \frac{M}{EI} \cdot \frac{t_{laminare}}{2}$$

Transposition equation (14) for moment M the strain energy of the skin derives to equation (16).

$$(15) M = \frac{2\epsilon E}{t_{laminare}} \cdot EI$$

$$(16) L_{skin} = \int_0^r 2 \frac{\pi(r + \frac{t_{laminare}}{2})}{t_{laminare}} \frac{E}{\pi r} \cdot EI \cdot \frac{l}{\pi r} dr$$

5.2.3. Strain energy determination of flexural adhesive

By the known translation of Points P_{1_2} and P_{2_2} and the corresponding Skin radiuses the internal loads and thus the Strain energy can be derived. The following Figure displays the assumed deformation.

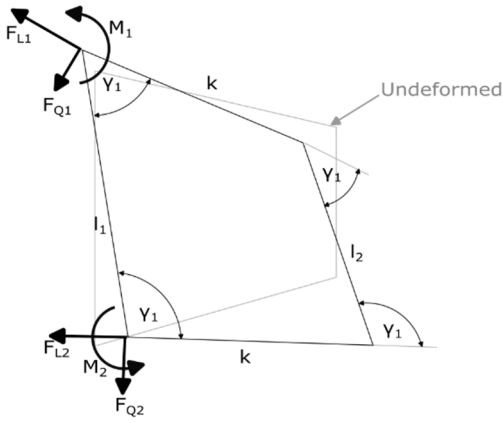


Figure 9: Model of the flexural adhesive where the skins are attached to the sides k

The length l_1 and l_2 connect the corners of the model. These distances can vary due to very small Young's modulus of the Flexural adhesive. The sides k cannot change due to comparable high modulus of the skins. Reaction forces of bonding according to the movement of the corners can be determined evaluating the elongation of sides l_1 and l_2 , by multiplication with the adhesives Young's modulus. The local forces in direction of l_1 and l_2 are known with the following equation.

$$(17) F_{n_internal} = \epsilon_n \cdot E_n = \frac{l_{n_deformed} - l_{n_undeformed}}{l_{n_undeformed}} E_n$$

The cut forces can derive by integrating the local forces over the upper and lower skin.

$$(18) F_L = \int_0^k F_{n_internal} \cdot \sin(\gamma) dk + G \cdot \gamma$$

$$(19) F_Q = \int_0^k F_{n_internal} \cdot \cos(\gamma) dk$$

$$(20) M = \int_0^k F_{n_internal} \cdot \cos(\gamma) \cdot k dk$$

To derive the strain energy a virtual force will be placed at the end of the pressure side, which will be derived by vertical static equilibrium. Due to small angles of δ deviation to vertical will be neglected.

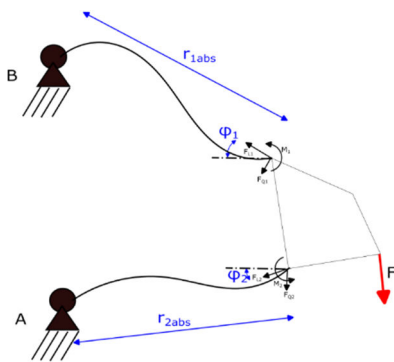


Figure 10: Model of the flexural adhesive with virtual force F and arbitrary skin deformation

$$(21) F = F_{Av} + F_{Bv}$$

$$(22) F_{Av} = -F_{L2} \sin(\varphi_2) + F_{Q2} \cos(\varphi_2) - M_2 r_2 \sin(\varphi_2)$$

$$(23) F_{Bv} = -F_{L1} \sin(\varphi_1) + F_{Q1} \cos(\varphi_1) - M_1 r_1 \sin(\varphi_1)$$

As φ is in both models dependent to δ the following formula can be stated.

$$(24) L_{flexure} = F(\delta) \cdot r \cdot \sin(\delta)$$

As this Model considers the bending stiffness of the skin as well as elongation of the flexural adhesive it is expected to reflect the Strain energy as well as the virtual load F more precisely compared to Model II. This Model is limited to medium size deformations due to assuming a deformed shape of the skins before solving the equations.

5.3. Model III

In contrast to the preliminary models the following approaches using high fidelity software tools basing on finite element theory.

An noncommercial tool chain has been set up by using Gmsh [3] for preprocessing and mesh generation and B2000++ [4] as FE-solver and Paraview [5] as postprocessor.

The mesh is generated by reading profile coordinate file, adding the lines for rear spar and the bounds of the flexural adhesive.

The 2D lines and the area of the flexural adhesive are than extruded to surfaces and volumes, which results in a structured meshed with quadratic shell elements (4 nodes) and cubic volume elements (8 nodes). Figure 11 shows the resulting mesh.

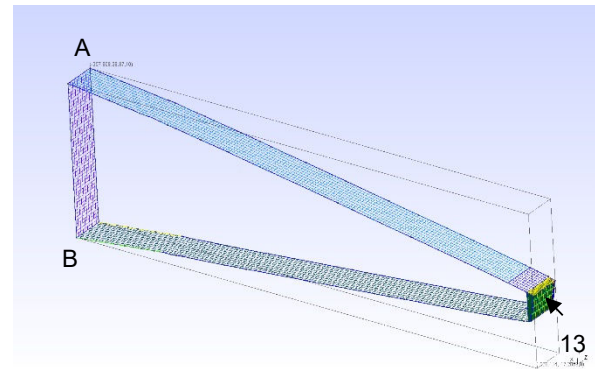


Figure 11: Finite element mesh of the trailing edge with a span of 10 mm and the rear spar between point A and point B

All suction- and pressure side surfaces are assigned with the same composite Materials. A composite material is also assigned to the rear spar surface. The volume elements are assigned with linear elastic material properties.

All nodes at the top and bottom line of the rear spar are fixed to all degrees of freedom (DOF). The lines at the side

of the profiles are fixed in y-direction. A deformation in z direction is applied to nodes of line 13. The solver setting is set to be geometrically nonlinear.

Large deformation lead to rotation of node coordinate systems around y so fixing x rotation in initial state yield to fixing of z Rotation in deformed state. B2000++ adopt boundary condition to each state of transient solution. That's why a small inaccuracy close to the y edges of the Model is expected. The elastic strain energy is evaluated by postprocessing the reaction force one node In the middle of load introduction line 13 multiplied by the deformation in z-direction.

5.4. Model IV

Up to now aerodynamic was not considered, because it is assumed that the structural internal load is dominant. This will be proven by this model.

Model IV is based on Model III, but it is extended by applying the aerodynamic pressure to the specific surface elements. The pressure distribution is derived by selecting a slice of the deformed solution and exporting the node positions to into Xfoil [6] in order to compute the pressure distribution for a given lift coefficient (C_a).

Since pressure is dependent to the deformed shape and vice versa the calculation of deformed shape needs to be iteratively.

The requirements of both systems are too different to be able to use the same elements and node positions for both systems. Therefore, the results of Xfoil need to be mapped on the structural mesh. Since Xfoil uses a lower number of elements it is decided to map the element pressures to the structural elements where the element middle points of the structural element is between the nodes of the aerodynamic elements. Figure 12 shows two kinds of error is by this procedure. Both are depending to the relative Positions of the mid points to the X-Foil nodes.

- shift of Pressures
- Area de- or increase for each Pressure Element of Xfoil.

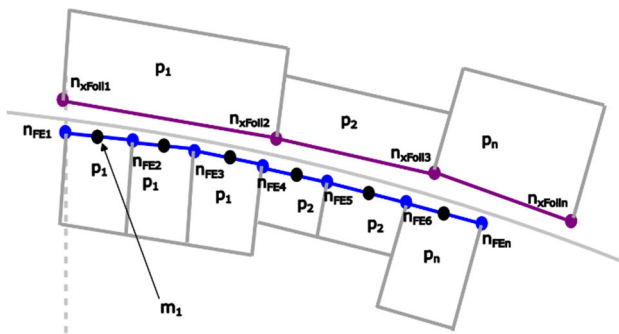


Figure 12: Pressure mapping scheme with purple nodes from Xfoil and blue nodes from FEM

Both types of errors reducing directly with the Quotient Xfoil elements number to FEM element number.

While the number of structural elements is much higher than the number of aerodynamical elements this error is decided to be neglectable.

The Boundaries used for Xfoil's pressure distribution is 1g level flight and VNE and Maximum deflected TE. Using ICAO standard atmosphere [7] at zero altitude and constant lift is used to derive the input data for Xfoil. As this is assumed to be the most critical condition from structural point of view.

Strain energy is obtained in identical to Procedure of Model III section 5.3.

6. RESULTS

First all results will be presented and discussed separately before concluding an overall image comparing the models.

6.1. Potential of HyTEM

Since fundamental potential of the trailing edge flexural adhesive is investigated by model I the following diagram in figure 13 shows the dimensionless internal force (F) quotient F_{flex}/F_{rigid} with respect to conventional design, which is to be assumed as rigid at the trailing edge. Therefore, a dimensionless force of 1 is equal to a rigid design. Figure 13 shows a strong dependency to χ , which is in the example of Proteus it is estimated to vary in the region between the purple (very soft Bonding) and red (harder bonding) vertical line.

Furthermore, it can be recognized that the internal loads are dependant to flexural adhesive thickness with $F \sim \frac{1}{t} \sim t^{-1}$ as this factors higher with decreasing χ . The internal loads can be reduced to 0,65 to 0,05 F depending to χ and $\tan t$. So a great potential can be found in this design to achieve a undisturbed profile skin.

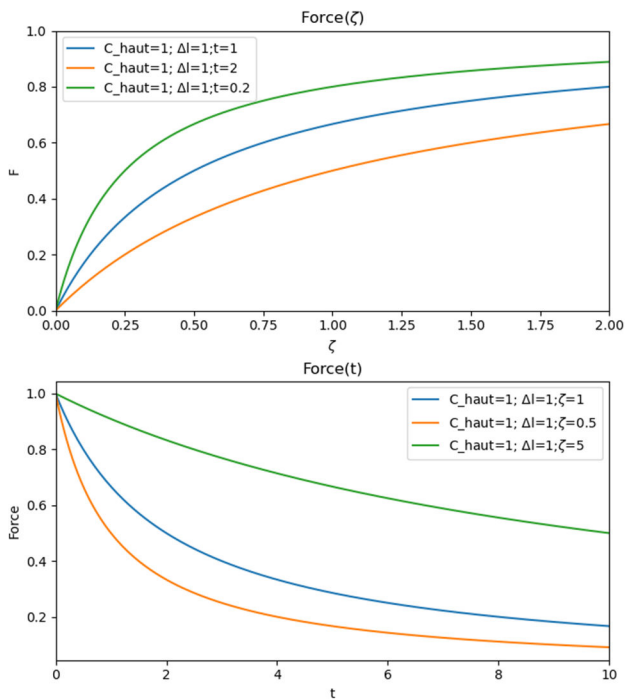


Figure 13: Potential Load reduction

6.2. Strain Energy

For number and sizing of actuators it is essential to fit the total strain energy of the system as well as the maximum required force at the load introduction point. Figure 14 shows the strain energy per millimeter of flap width over the absolute excitation of the trailing flap tip. The y-direction is heading downwards.

Figure 14 shows for all models an exponential growth with rising deformation of the structure.

Model I and model II showing higher values than the high-fidelity models III and IV.

Model II has higher strain energy below 22mm and lower energy in higher deflection compared to Model I. This can be conducted by storing strain energy in the skins is significant at lower deflection due to small deflections of the flexural adhesive in this situation. At higher deflection the differences of Δl and deviating trajectories shown in Figure 7 lead to a lower increase of the energy.

The deviation between the analytical and FE models can be explained by different shapes of deformation in both results. As in the analytical approaches a stiff hinged or circle segments are assumed in Model III and IV the shape might be more complex with the lowest strain energy possible stored in the system.

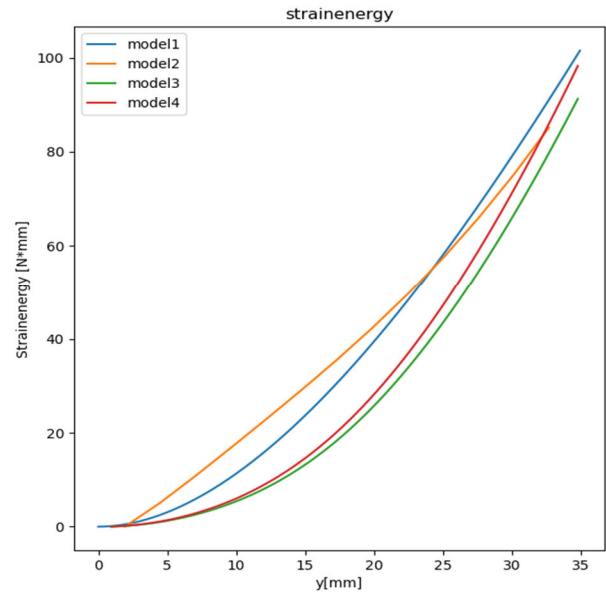


Figure 14: Strainenergy

Additionally these differing shapes lead to an different and smaller Shear deformation of the flexural adhesive. Which is furthermore reducing streinenergy.

The required virtual reaction force diagram can be found in Figure 15. In this diagram the virtual reaction force-flow (Force per millimeter flap width) over the profile excitation is shown. It is noticeable that the analytical and the high fidelity models showing different curve characteristics.

It can be recognized that model IV results into the highest force flows as model II showing the smallest absolute maximal values. At maximum deflection the deviation of 1,4 N/mm Between Model II and Model III is considerable for total drive sizing. Different shapes of curvature of model I to model III and IV is also recognizable. As model I shows substantial higher loads for smaller deformation but lower for higher deformation.

Using model I for preliminary design will provide a conservative overall sizing method, which allows parameter studies for a wide branch of design parameters concerning the flexural adhesives and the actuators, but not the skin and transition design itself.

[7] ICAO, "Manual of the ICAO Standard Atmosphere - extended to 80 kilometres / 262,500 feet (Doc. 7488)," ICAO, 1978.

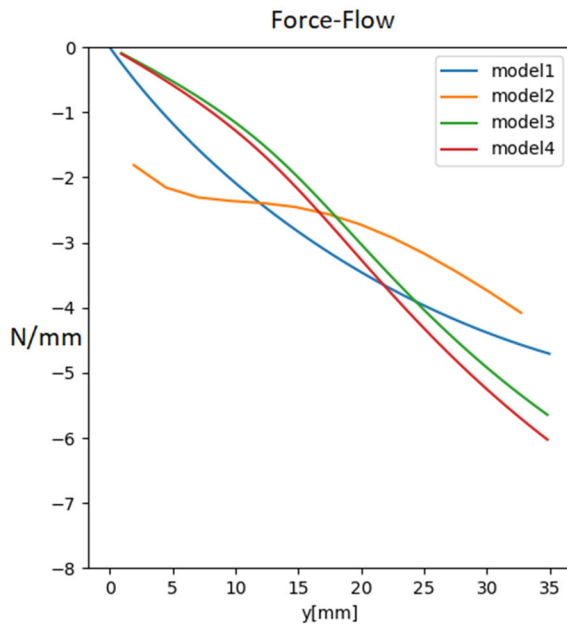


Figure 15: Virtual Force-flow

The models I and II are appropriate for choosing actuator size and numbers.

High deviation in deformation and force of the high-fidelity models indicates that Model I and II are not appropriate for selecting transmission and their potential weight.

Furthermore, models I and II are not able to indicate instabilities of the skins. These methods have to be applied in further steps to reach a proper design of a morphing trailing edge.

7. REFERENCES

- [1] Barbarino, S., Bilgen, O., Ajaj, R. M., Friswell, M. I., and Inman, D. J., "A Review of Morphing Aircraft," *Journal of Intelligent Material Systems and Structures*; Vol. 22, No. 9, 2011, pp. 823–877. doi: 10.1177/1045389X11414084.
- [2] do Vale, J. L., Afonso, F., Lau, F., and Suleman, A., "Span Morphing Concept: An Overview," *Morphing Wing Technologies*, Elsevier, 2018, pp. 125–144.
- [3] Geuzaine, C., and Remacle, J.-F., *Gmsh*, 2022.
- [4] Boer, A. de, and Riks, E., "The nonlinear analysis part of B2000: A first evaluation," NLR TR / Nationaal Lucht- en Ruimtevaartlaboratorium NLR TR 88109 U, 1988.
- [5] Ayachit, U., *The ParaView guide. A parallel visualization application*; updated for ParaView version 4.3, Kitware, Clifton Park, NY, 2015.
- [6] Drela, M., ed., *Xfoil: An Analysis and Design System for Low Reynolds Number Airfoils*, MIT, 1989.